The mass of the Milky Way from satellite dynamics

Thomas M. Callingham,[1] Marius Cautun [ID],[1] Alis J. Deason [ID],[1] Carlos S. Frenk,[1]
Wenting Wang,[2] Facundo A. Gómez,[3,4] Robert J. J. Grand [ID],[5,6] Federico Marinacci [ID][7]
and Ruediger Pakmor [ID][5]

[1]*Institute of Computational Cosmology, Department of Physics, University of Durham, South Road, Durham DH1 3LE, UK*
[2]*Kavli IPMU (WPI), UTIAS, The University of Tokyo, Kashiwa, Chiba 277-8583, Japan*
[3]*Instituto de Investigación Multidisciplinar en Ciencia y Tecnología, Universidad de La Serena, Raúl Bitrán 1305, La Serena, Chile*
[4]*Departamento de Física y Astronomía, Universidad de La Serena, Av. Juan Cisternas 1200 N, La Serena, Chile*
[5]*Heidelberger Institut für Theoretische Studien, Schloss-Wolfsbrunnenweg 35, D-69118 Heidelberg, Germany*
[6]*Zentrum für Astronomie der Universität Heidelberg, ARI, Mönchhofstr. 12-14, D-69120 Heidelberg, Germany*
[7]*Department of Physics, Kavli Institute for Astrophysics and Space Research, MIT, Cambridge, MA 02139, USA*

ABSTRACT

We present and apply a method to infer the mass of the Milky Way (MW) by comparing the dynamics of MW satellites to those of model satellites in the EAGLE cosmological hydrodynamics simulations. A distribution function (DF) for galactic satellites is constructed from EAGLE using specific angular momentum and specific energy, which are scaled so as to be independent of host halo mass. In this two-dimensional space, the orbital properties of satellite galaxies vary according to the host halo mass. The halo mass can be inferred by calculating the likelihood that the observed satellite population is drawn from this DF. Our method is robustly calibrated on mock EAGLE systems. We validate it by applying it to the completely independent suite of 30 AURIGA high-resolution simulations of MW-like galaxies: the method accurately recovers their true mass and associated uncertainties. We then apply it to 10 classical satellites of the MW with six-dimensional phase-space measurements, including updated proper motions from the *Gaia* satellite. The mass of the MW is estimated to be $M_{200}^{\mathrm{MW}} = 1.17_{-0.15}^{+0.21} \times 10^{12}\,\mathrm{M_\odot}$ (68 per cent confidence limits). We combine our total mass estimate with recent mass estimates in the inner regions of the Galaxy to infer an inner dark matter (DM) mass fraction $M^{\mathrm{DM}}(< 20\,\mathrm{kpc})/\mathrm{M}_{200}^{\mathrm{DM}} = 0.12$, which is typical of $\sim 10^{12}\,\mathrm{M_\odot}$ lambda cold dark matter haloes in hydrodynamical galaxy formation simulations. Assuming a Navarro, Frenk and White (NFW) profile, this is equivalent to a halo concentration of $c_{200}^{\mathrm{MW}} = 10.9_{-2.0}^{+2.6}$.

Key words: methods: data analysis – Galaxy: halo – galaxies: dwarfs – galaxies: haloes – galaxies: kinematics and dynamics – .

1 INTRODUCTION

The mass of the Milky Way (MW) is a fundamental astrophysical parameter. It not only is important for placing the MW in context within the general galaxy population, but also plays a major role when trying to address some of the biggest mysteries of modern astrophysics and cosmology. The intricacies of galaxy formation are highly dependent on feedback and star formation processes, which undergo a crucial physical transition around the MW mass (e.g. Bower et al. 2017). Apparent discrepancies with the standard lambda cold dark matter (ΛCDM) model, such as the missing

satellites (Klypin et al. 1999; Moore et al. 1999) and the too-big-to-fail problems (Boylan-Kolchin, Bullock & Kaplinghat 2011), depend strongly on the MW halo mass (e.g. Purcell & Zentner 2012; Wang et al. 2012; Vera-Ciro et al. 2013; Cautun et al. 2014a). In addition, tests of alternative warm dark matter (DM) models (Kennedy et al. 2014; Lovell et al. 2014) are also subject to the total halo mass. Thus, by considering the cosmological context of the MW and its population of dwarf galaxy satellites, important inferences about large-scale cosmology can be made. With the recent *Gaia* DR2 release (Gaia Collaboration 2018a), we now have significantly more information than ever before about our galaxy, and are better placed to make progress on these problems.

There have been many attempts to infer directly the MW mass through a variety of methods. The total MW mass is dominated by its

DM halo, which cannot be observed directly. Instead, its properties must be inferred from the properties of luminous populations, such as the luminosity function of MW satellites (mostly the Large and Small Magellanic Clouds, *LMC* and *SMC*; e.g. Busha et al. 2011b; González, Kravtsov & Gnedin 2013; Cautun et al. 2014b) and the kinematics of various dynamical tracers of the Galactic halo. The dynamics of halo tracers are mostly determined by the gravitational potential of the MW halo, and provide a key indirect probe of the total halo mass. Examples of halo tracers used for this purpose are satellite galaxies (e.g. Wilkinson & Evans 1999; Watkins, Evans & An 2010), globular clusters (e.g. Eadie & Harris 2016; Binney & Wong 2017; Sohn et al. 2018; Watkins et al. 2018), halo stars (e.g. Xue et al. 2008; Deason et al. 2012; Kafle et al. 2012, 2014), high-velocity stars (e.g. Smith et al. 2007; Piffl et al. 2014; Fragione & Loeb 2017; Rossi et al. 2017; Monari et al. 2018), and stellar streams (e.g. Koposov, Rix & Hogg 2010; Newberg et al. 2010; Gibbons, Belokurov & Evans 2014; Bowden, Belokurov & Evans 2015; Küpper et al. 2015).

There are a variety of methods for inferring the Galactic halo mass using dynamical tracers. A common approach is to model the tracers as distributions in equilibrium whose parameters are determined by fitting the model to observational data (e.g. Evans et al. 2003; Han et al. 2016a). Advances in the calculation of action-angle coordinates (e.g. Vasiliev 2019) have led to a new generation of analytical galaxy modelling, centred around distribution functions (DFs) in action-angle space. Examples include modelling the MW population of globular clusters (e.g. Posti & Helmi 2018) or individual DFs of components such as the thick and thin disc, bulge, stellar halo, and DM halo (Cole & Binney 2017). The recent availability of large cosmological simulation has enabled a new class of methods based on comparing the observed properties of MW satellites to those of substructures in cosmological simulations (e.g. Busha et al. 2011a; Patel, Besla & Mandel 2017).

Although over the past decades a large amount of effort has been dedicated to inferring the Galactic halo mass, its value remains uncertain to within a factor of 2, with most mass estimates ranging from 0.5×10^{12} to $2.5 \times 10^{12}\,\mathrm{M}_\odot$ (e.g. Wang et al. 2015, and our Fig. 7). While many studies claim uncertainties smaller than this range, the analytical models upon which they rely require several assumptions such as dynamical equilibrium and a given shape of the density or the velocity anisotropy profiles. These assumptions can lead to additional systematic errors, which are difficult to quantify but can be the dominant source of error (e.g. see Yencho et al. 2006; Wang et al. 2015, 2018). This is especially true for the MW halo whose dynamics are likely to be affected by the presence of a very massive satellite, the *LMC* (Gómez et al. 2015; Peñarrubia et al. 2016; Shao et al. 2018c). Furthermore, most methods typically estimate the mass within the inner tens of kiloparsecs, since this is the region where most tracers (such as halo stars and globular clusters) reside, necessitating an extrapolation to the virial radius. This extrapolation requires additional assumptions about the radial density profile of the MW and can lead to further systematic uncertainties.

Large-volume high-resolution cosmological simulations offer a unique test-bed for analytical mass determination methods (e.g. Han et al. 2016b; Peñarrubia & Fattahi 2017; Wang et al. 2017) and, importantly, enable new methods for inferring the Galactic halo mass with a minimal set of assumptions. The simulations have the advantage of self-consistently capturing the complexities of halo and galaxy formation, as well as the effects of halo-to-halo variation. However, with a few exceptions, the limited

mass resolution of current simulations means that they can resolve satellite galaxies but not halo stars or globular clusters (although see e.g. Grand et al. 2018; Pfeffer et al. 2018). This is not a major limitation since satellite galaxies, due to their radially extended spatial distribution, are one of the best probes of the outer MW halo. This is especially true now that the *Gaia* DR2 release has provided a large sample of MW satellites with full six-dimensional phase space information (Fritz et al. 2018; Gaia Collaboration 2018b; Simon 2018).

Galactic halo mass estimates that rely on cosmological simulations are relatively recent. Busha et al. (2011a) pioneered the approach of inferring halo properties by finding the best match between the MW satellites and satellites of simulated haloes. The MW mass is then determined by weighting the host haloes according to the quality of the satellite match, a technique known as importance sampling. Busha et al. used the distance, velocity, and size of the *LMC* and *SMC* to constrain the MW mass. The distance and velocity of satellites can vary rapidly, especially when close to the pericentre of their orbit, so very large simulations are needed in order to find enough counterparts to the MW system.

Patel et al. (2017) pointed out that approximately conserved quantities, such as angular momentum, are better for identifying satellite analogues in simulations. This makes it easier to find MW counterparts; applying the criterion to a larger number of satellites results in a more precise mass determination (Patel et al. 2018). A further advance was achieved by Li et al. (2017), who showed that, when scaled appropriately, the DF of satellite energy and angular momentum becomes independent of halo mass. This scaling allows for a more efficient use of simulation data, since any halo can be rescaled to a different mass, and thus a better sampling of halo formation histories and halo-to-halo variation can be achieved. This approach represents a major improvement over importance sampling methods, in which the statistically relevant systems are those in a small mass range.

In this paper we improve and extend the Li et al. (2017) mass determination method. We start by constructing the phase-space distribution of satellite galaxies using a very large sample of host haloes taken from the EAGLE (Evolution and Assembly of GaLaxies and their Environments) galaxy formation simulation (Crain et al. 2015; Schaye et al. 2015). We then describe and calibrate three mass inference methods based on the satellite distributions of (i) angular momentum only, (ii) energy only, and (iii) a combination of both angular momentum and energy. We test these methods by applying them to an independent set of simulations, taken from the AURIGA project (Grand et al. 2017); this is a very stringent test because of the much higher resolution and rather different galaxy formation model implemented in AURIGA compared to EAGLE. Finally, we apply our methods to the latest observations of the classical satellites to determine the MW halo mass; we are able to estimate this mass with an uncertainty of only 20 per cent.

The structure of the paper is as follows. Section 2 describes the construction of the phase-space DFs using the EAGLE data. Section 3 describes our mass inference methods, their calibration, and validation with tests on mock systems. In Section 4, we apply this method to the observed MW system and discuss our results. Finally, Section 5 summarizes and concludes the paper.

2 CONSTRUCTION OF THE SATELLITE DISTRIBUTION

We now describe how to obtain a phase space distribution of satellites that, when scaled appropriately, is independent of host halo

mass. We then introduce the MW observations, and the simulation data that we use for calculating the phase-space DF of satellite galaxies.

2.1 Theoretical background

We are interested in the energy and angular momentum distribution of Galactic satellites. This can be calculated starting from the observed distance, r^s, tangential velocity, v_t^s, and speed, v^s, of satellite s, which we use to define the vector:

$$\boldsymbol{x}^s = \left(v^s, v_t^s, r^s\right). \tag{1}$$

The specific energy, E, and specific angular momentum, L, of a satellite are given by

$$E = \frac{1}{2}|\mathbf{v}|^2 + \Phi(r)$$
$$L = |\boldsymbol{r} \times \boldsymbol{v}| = r v_t, \tag{2}$$

where $\Phi(r)$ is the gravitational potential at the position of the satellite. This cannot be measured directly in observations, and to calculate it, we need to assume a mass profile for the host halo. Here, we assume that the host density profile is well approximated by a spherically symmetric Navarro, Frenk and White profile (hereafter NFW; Navarro, Frenk & White 1996, 1997), whose gravitational potential is given by

$$\Phi_{\mathrm{NFW}}(r) = -\frac{GM_{200}}{r} \frac{\ln\left(1 + C\frac{r}{R_{200}}\right)}{\ln(1+C) - \frac{C}{C+1}}, \tag{3}$$

where C is the concentration of the halo and M_{200} and R_{200} denotes the halo mass and radius, respectively. The mass, M_{200}, corresponds to the mass enclosed within a sphere of average density 200 times the critical density.

The NFW profile provides a good description of the radial density profile of relaxed haloes in DM-only simulations. The addition of baryons leads to a contraction of the inner region of haloes, and thus to a systematic departure from an NFW profile (e.g. Gnedin et al. 2004). However, at large enough distances (e.g. $r \gtrsim 20$ kpc for a halo mass of 10^{12} M$_\odot$) the NFW profile still provides a very good description of the mass distribution even in galaxy formation simulations (e.g. Schaller et al. 2015; Zhu et al. 2016). In this work, we consider only satellites relatively far from the halo centre, where the NFW function represents a good approximation of the mass profile.

DM haloes have several self-similar properties, such as their density profiles (e.g. Navarro et al. 1996, 1997), the substructure mass function (e.g. Wang et al. 2012; Cautun et al. 2014a), and the radial number density of subhaloes (Springel et al. 2008; Hellwing et al. 2016). Li et al. (2017) showed that the same self-similar behaviour also holds for the energy and angular momentum DFs of subhaloes. This implies that, when scaled accordingly, satellites around hosts of different mass follow the same energy and angular momentum distribution. The same self-similar behaviour also holds to a good approximation in the EAGLE hydrodynamic simulation (see Appendix B).

For a self-similar halo density profile, the satellites' positions and velocities scale with $M_{200}^{1/3}$ (Li et al. 2017). A given host halo and its associated satellite system can therefore be scaled to a different host halo mass, M_{200}^{Scale}, as

$$\left(r', v', v_t'\right) = \left(\frac{M_{200}^{\mathrm{Scale}}}{M_{200}}\right)^{\frac{1}{3}} (r, v, v_t). \tag{4}$$

Table 1. Properties of the classical Galactic satellites used in this work. The last two columns give the calculated energy and angular momentum values for each satellite. The energy has been calculated using an NFW profile with a concentration of 8, for a mass, $M_{200}^{\mathrm{MW}} = 1.17 \times 10^{12}$ M$_\odot$, which corresponds to our best MW-halo mass estimate. The distance is with respect to the Galactic Centre. The specific orbital angular momentum, L, and specific energy, E, of the satellites are expressed in terms of the angular momentum, $L_{0;\,\mathrm{MW}}$, and energy, $E_{0;\,\mathrm{MW}}$, of a circular orbit at the virial radius, R_{200}. For the mass and concentration assumed here, we have $L_{0;\,\mathrm{MW}} = 3.34 \times 10^4$ kpc km s^{-1} and $E_{0;\,\mathrm{MW}} = 2.28 \times 10^4$ km^2 s^{-2}. The errors give the 68% confidence interval based on the Monte Carlo sampling of the observational errors (see the text for details).

Satellite	Distance [kpc]	$L/L_{0;\,\mathrm{MW}}$	$E/E_{0;\,\mathrm{MW}}$
LMC	51 ± 2	$0.46^{+0.05}_{-0.05}$	$-1.33^{+0.32}_{-0.31}$
SMC	64 ± 4	$0.46^{+0.08}_{-0.08}$	$-1.84^{+0.42}_{-0.37}$
Draco	76 ± 6	$0.30^{+0.03}_{-0.03}$	$-2.40^{+0.10}_{-0.11}$
Ursa Minor	76 ± 6	$0.32^{+0.02}_{-0.01}$	$-2.39^{+0.05}_{-0.05}$
Sculptor	86 ± 6	$0.48^{+0.03}_{-0.03}$	$-1.89^{+0.07}_{-0.07}$
Sextans	86 ± 4	$0.67^{+0.06}_{-0.05}$	$-1.21^{+0.17}_{-0.16}$
Carina	105 ± 6	$0.55^{+0.08}_{-0.08}$	$-1.86^{+0.19}_{-0.19}$
Fornax	147 ± 12	$0.70^{+0.21}_{-0.19}$	$-1.52^{+0.33}_{-0.30}$
Leo II	233 ± 14	$0.96^{+0.30}_{-0.28}$	$-1.20^{+0.29}_{-0.21}$
Leo I	254 ± 15	$0.82^{+0.28}_{-0.26}$	$-0.67^{+0.21}_{-0.15}$

This implies that the energy and angular momentum of satellites also scale with halo mass through the relation $E, L \propto M_{200}^{2/3}$. Thus, we can choose characteristic E_0 and L_0 values for each halo mass and use them to rescale the E and L values of each satellite to obtain mass independent quantities. For each halo, we define the scaled specific energy, $\widetilde{E}$, and scaled specific angular momentum, $\widetilde{L}$, as

$$\left(\widetilde{E}, \widetilde{L}\right) = \left(\frac{E}{E_0}, \frac{L}{L_0}\right), \tag{5}$$

where the characteristic E_0 and L_0 values correspond to the energy and angular momentum of a circular orbit at R_{200} and are given by

$$E_0 = \frac{GM_{200}}{R_{200}}$$
$$L_0 = \sqrt{GM_{200}R_{200}}. \tag{6}$$

This scaling relation preserves the relaxation state, concentration, and formation history of the halo, giving scaled properties that are independent of host mass (see Appendix B).

2.2 Observational data for the MW satellites

We aim to estimate the MW halo mass using the classical satellites since those have the best proper motion measurements. The method we employ is flexible enough to incorporate the ultrafaint dwarfs; however, the EAGLE simulation, which we use for calibration does not resolve the ultrafaint satellites. Furthermore, we discard any satellites closer than 40 kpc (see Section 2.3), so we exclude the *Sagittarius* dwarf from our observational sample. *Sagittarius* is currently at a distance of 26 kpc, undergoing strong tidal disruption by the MW disc, and is therefore unsuitable as a tracer of the DM halo. This leaves 10 classical satellites with adequate kinematical data (see Table 1).

We take satellite positions, distances, and radial velocities from the McConnachie (2012) compilation. We use the observed proper motions of the classical satellites derived from the *Gaia* data

release DR2 (Gaia Collaboration 2018b), apart from the most distant satellites, *Leo I* and *Leo II*, for which we use the *Hubble Space Telescope* proper motions (Sohn et al. 2013; Piatek, Pryor & Olszewski 2016) since these have smaller uncertainties.

To calculate the energy and angular momentum, we transform the satellite positions and velocities from Heliocentric to Galactocentric coordinates using the procedure described in Cautun et al. (2015). The transformation depends on the Sun's position and velocity for which we adopt: $d = 8.29 \pm 0.16$ kpc for the distance of the Sun from the Galactic Centre; $V_{\rm circ} = 239 \pm 5$ km s^{-1} for the circular velocity at the Sun's position (McMillan 2011); and $(U, V, W) = (11.1 \pm 0.8, 12.2 \pm 0.5, 7.3 \pm 0.4)$ km s^{-1} for the Sun's motion with respect to the local standard of rest (Schönrich, Binney & Dehnen 2010). When transforming to Galactocentric coordinates, we account for errors in the distance, radial velocity, and proper motion of each satellite, as well as in the Sun's position and velocity, which we model as normally distributed errors. To propagate the errors, we generate a set of 1000 Monte Carlo realizations of the MW system in heliocentric coordinates and transform each realization to Galactocentric coordinates.

2.3 EAGLE simulation sample

We select our sample of host haloes and satellite populations from the reference run of the EAGLE project (Crain et al. 2015; Schaye et al. 2015). The simulation follows galaxy formation in a 100 Mpc cubic volume with the *Planck* cosmological parameters (Planck Collaboration I 2014, see table 9) using 1504^3 DM particles of mass of 9.7×10^6 M$_\odot$ and 1504^3 gas particles of initial mass of 1.81×10^6 M$_\odot$. EAGLE models the relevant baryonic physics processes such as gas cooling, stochastic star formation, stellar and AGN feedback, and the injection of metals from supernovae and stellar winds; it was calibrated to reproduce the present-day stellar mass function, galaxy sizes, and the galaxy mass–black hole mass relation. The population of haloes and subhaloes was identified using the SUBFIND algorithm (Springel, Yoshida & White 2001). The large volume of the EAGLE simulation provides a large sample of haloes, of a wide range of masses and assembly histories. Our final sample consists of the following host haloes and satellites galaxies.

Selection criteria for hosts haloes:

(i) Halo mass, M_{200}, in the range $10^{11.7}$–$10^{12.5}$ M$_\odot$;

(ii) relaxed systems, that is haloes for which the distance between the centre of mass and the centre of potential is less than $0.07R_{200}$ and the total mass in substructures is less than 10 per cent (Neto et al. 2007).

Selection criteria of satellite galaxies:

(i) Distance from halo centre in the range 40 kpc $< r' <$ 300 kpc, where $r' = r(10^{12}\,{\rm M}_\odot/M_{200})^{1/3}$ is the rescaled distance of the satellite corresponding to a halo of mass 10^{12} M$_\odot$ (see equation 4); this results in a similar radial distribution as the MW satellites if the MW halo had a mass of 10^{12} M$_\odot$;

(ii) the satellite is luminous, i.e it contains at least one star particle, which excludes dark subhaloes.

This gives a sample of approximately ∼1, 200 host haloes and ∼14 000 satellites. Our mass scaling method allows us to choose haloes in a broad mass range. The restriction on the radial
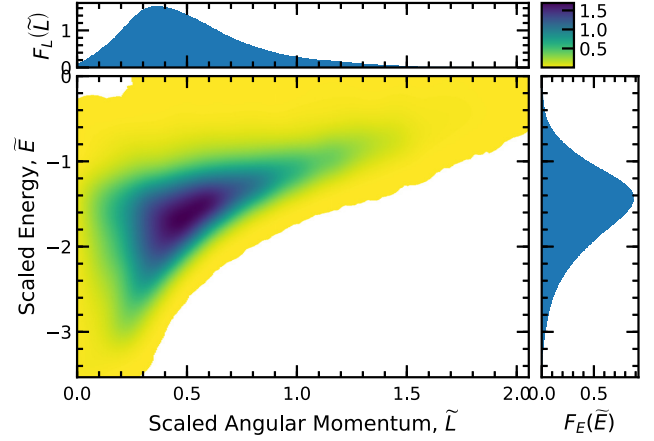

Figure 1. The distribution, $F(\widetilde{E}, \widetilde{L})$, of bound EAGLE satellites in terms of the scaled angular momentum, $\widetilde{L}$, and scaled energy, $\widetilde{E}$. The energy and angular momentum are scaled according to equation (5) to obtain quantities that are independent of host halo mass, M_{200}. The colour gives the number density of satellites, with dark colours corresponding to higher number densities (see colour bar). The two side panels show the one-dimensional distributions of the scaled energy $F_E(\widetilde{E})$ (right-hand panel) and scaled angular momentum $F_L(\widetilde{L})$ (top panel) of satellites.

distribution of satellite galaxies is chosen so that the model samples match the observed one and to ensure that the potential is dominated by DM.

In Fig. 1 we show the distribution of EAGLE satellites in scaled energy and angular momentum space, $(\widetilde{E}, \widetilde{L})$. For each satellite, we calculate the energy by assuming that the host halo is well described by an NFW profile individually fitted to each halo as described in Schaller et al. (2015). This procedure is similar to how energy is calculated for observational satellites, and thus allows for a proper comparison between theory and observations. To obtain a continuous DF, we applied a 2D Gaussian smoothing with dispersions $\alpha\sigma_{\widetilde{L}}$ and $\alpha\sigma_{\widetilde{E}}$ for the $\widetilde{L}$ and $\widetilde{E}$ directions, respectively. The symbols $\sigma_{\widetilde{L}} = 0.36$ and $\sigma_{\widetilde{E}} = 0.52$ denote the standard deviation of the $\widetilde{L}$ and $\widetilde{E}$ distributions, respectively. The parameter $\alpha = 0.125$ was chosen as a compromise so as to obtain a locally smooth function without significantly changing the overall shape of the DF.

The distribution in $(\widetilde{E}, \widetilde{L})$ space is not uniform and satellites are most likely to have values around the peak of the DF, $(\widetilde{E}, \widetilde{L}) \approx (-1.5, 0.5)$, which corresponds to the dark coloured region in Fig. 1. The $(\widetilde{E}, \widetilde{L})$ distribution is bounded on the lower right-hand side by circular orbits. Moving perpendicularly away from this boundary, the orbits become increasingly radial. The $\widetilde{E}$ distribution is bounded by the potential energy of the inner radial cut, and the $\widetilde{L}$ distribution is bounded by a circular orbit at the outer radial cut. In our sample, approximately 1 per cent of the satellites are unbound, i.e $E > 0$, which is consistent with previous studies (Boylan-Kolchin et al. 2013). However, we note that we do not calculate the exact binding energy of each satellite, but only an approximate value under the assumption that the host halo is spherically symmetric and well described by an NFW profile (see equation 3). While not shown in Fig. 1, we do keep unbound satellites in our analysis and thus we make no explicit assumption that MW satellites, such as *Leo I*, are bound. Instead, it is simply improbable that *Leo I* is unbound, and this is reflected in the individual satellites mass estimates we present in Section 4.

There are several advantages to obtaining a composite DF that is averaged over many host haloes instead of calculating individual

distributions for each halo, as done by Li et al. (2017). In EAGLE, the mass resolution limits the number of subhaloes that can be identified in each system. As a result, the satellite population of each system represents a poor sampling of their haloes unique DF. The total composite DF contains many possible halo histories, and their multiplicity effectively serves as a prior probability. With further knowledge of the MW's assembly history, it would be possible to restrict the model sample to have similar assembly histories to the MW. This could reduce the effective halo scatter and potentially result in a more accurate mass estimate. However, in this work we choose not to be too restrictive.

3 METHOD

We present three different methods for inferring the mass of the MW, each based on the following satellite properties: (i) orbital angular momentum, (ii) orbital energy, and (iii) both angular momentum and energy. All three methods employ the same principles and steps. We focus the discussion on the third method, which combines both L and E, and which should give the best mass constraints since it uses the largest amount of information. The methods we use are based on the approach of Li et al. (2017), which we have modified to work with a large sample of haloes and our mass independent DF, $F(\widetilde{E}, \widetilde{L})$.

We are interested in determining the mass of a host halo starting from the observed position and velocities of a set of N_{Sat} satellites. Each satellite, s, has a set of observed phase-space coordinates:

$$\mathbf{x}^s = \left(v^s, v_{\mathrm{t}}^s, r^s\right) \{\mathbf{x}^s\}_{s \in [0, N_{\mathrm{Sat}}]}, \tag{7}$$

consisting of the speed, v, the tangential velocity component, v_{t}, and the distance, r, from the host centre. These properties, combined with assumptions about the mass, M_{200}, and the density profile of the host, are sufficient to calculate the energy and angular momentum, $\left\{\widetilde{E}^s, \widetilde{L}^s\right\}\big|_{M_{200}}$, of each satellite. Varying M_{200} gives a path in the $(\widetilde{E}, \widetilde{L})$ plane for each satellite. As a function of M_{200}, $\widetilde{L}$ scales as $M_{200}^{-2/3}$ and so decreases asymptotically to zero for increasing value of M_{200}. The scaled energy, $\widetilde{E}$, has two terms that scale differently; the kinetic term scales as $M_{200}^{-2/3}$, while the potential term scales as $M_{200}^{1/3}$. With increasing M_{200}, the potential term dominates and $\widetilde{E}$ tends to $-\infty$.

Fig. 2 illustrates the path of the Galactic satellites in the $(\widetilde{E}, \widetilde{L})$ plane as we vary the assumed mass of the MW halo. For example, as we increase the value of M_{200}, the *LMC* dwarf moves from the top part of the plot to the bottom-left corner. This is because both $\widetilde{L}$ and $\widetilde{E}$ decrease with increasing M_{200} values.

The trajectory of the satellites through the 2D plane depends on the satellites' orbital phase. The scaled angular momentum, $\widetilde{L}$, varies as a function of M_{200} uniformly throughout the orbit, but the rate of change of the scaled energy, $\widetilde{E}$, is dependent on the satellites' current radius. Nearer pericentre, the satellites have higher absolute values of kinetic and potential energy components compared to those at larger distances. When increasing M_{200}, the scaled kinetic energy decreases while the absolute value of the scaled potential energy increases, causing the total scaled energy, $\widetilde{E}$, to decrease rapidly and thus results in a more vertical trajectory. The figure also illustrates that when the assumed M_{200} is very high, $\widetilde{L}$ varies slowly and so the paths become nearly vertical.

Fig. 2 illustrates how the energy and angular momentum of satellites can be used to determine the host halo mass. The DF in $(\widetilde{E}, \widetilde{L})$ space is not uniform, and as the assumed M_{200} of the host is varied, satellites move between regions of high and low
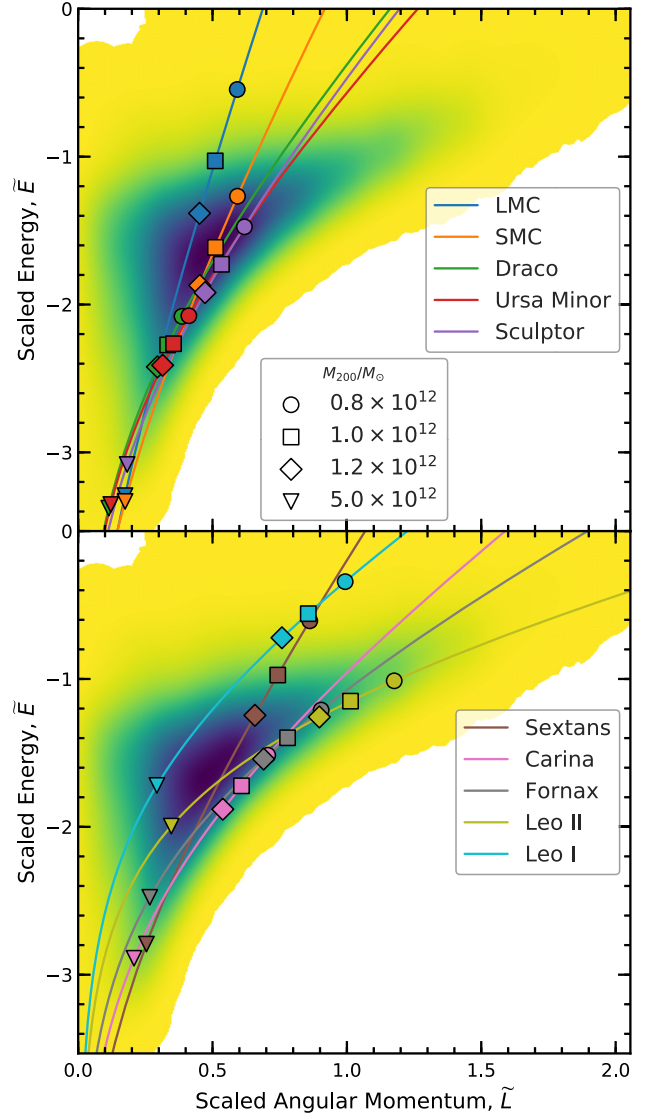

Figure 2. The path of the Galactic satellites in scaled energy – angular momentum space, $(\widetilde{E}, \widetilde{L})$, when varying the MW halo mass, M_{200}. Each curve corresponds to a different satellite (see the legend). The filled symbols show the location corresponding to the four values of M_{200} given in the legend. The energy has been calculated using an NFW profile with a concentration of 8. The colour scheme is the same as in Fig. 1, with darker colours corresponding to higher number densities.

number density in this space. For example, the *LMC* falls in a high-density region for $M_{200} \approx 1.4 \times 10^{12}$ M$_\odot$, and in lower density regions for higher or lower masses. Thus, the *LMC* phase space coordinates would prefer an MW halo mass of $\approx 1.4 \times 10^{12}$ M$_\odot$. In contrast, the *Leo I* path is nearest to the maximum density for $M_{200} \approx 2.9 \times 10^{12}$ M$_\odot$, and suggests a higher MW mass.

We now describe how each satellite can be used to obtain a likelihood for the MW halo mass, and how to combine the mass estimates from various satellites. Our aim is to determine the likelihood, $p(M_{200}|\mathbf{x}^s)$, for the host mass, given the observed $\mathbf{x}^s$ properties of satellite s.

The likelihood can be calculated from the $\widetilde{E}$ distribution via

$$p(M_{200}|\mathbf{x}^s) = F_E(\widetilde{E}) \left.\frac{\partial \widetilde{E}}{\partial M_{200}}\right|_{\widetilde{E} = \widetilde{E}^s}, \tag{8}$$

where the $F_E(\widetilde{E})$ term denotes the DF, while the partial derivative arises from the Jacobian of the transformation from $\widetilde{E}$ to host halo mass, M_{200}. The same procedure can be used to estimate the host mass using only the angular momentum by replacing $F_E(\widetilde{E})$ by the $\widetilde{L}$ DF, $F_L(\widetilde{L})$, and by changing the $\widetilde{E}$ derivative term to $\widetilde{L}$, to obtain

$$p(M_{200}|\mathbf{x}^s) = F_L(\widetilde{L}) \left. \frac{\partial \widetilde{L}}{\partial M_{200}} \right|_{\widetilde{L}=\widetilde{L}^s} . \qquad (9)$$

This expression can be extended to the two-dimensional case, where we use both $(\widetilde{E}, \widetilde{L})$ to constrain the halo mass, via

$$p(M_{200}|\mathbf{x}^s) = F(\widetilde{E}, \widetilde{L}) \, M_{200} \left. \frac{\partial \widetilde{E}}{\partial M_{200}} \frac{\partial \widetilde{L}}{\partial M_{200}} \right|_{\widetilde{E}=\widetilde{E}^s; \, \widetilde{L}=\widetilde{L}^s} , \qquad (10)$$

where the additional M_{200} factor is needed to have the correct units. Note that all the $\widetilde{E}$ and $\widetilde{L}$ terms in equations (8)–(10) are evaluated at the point $\widetilde{E}^s \equiv \widetilde{E}(\mathbf{x}^s, M_{200})$ and $\widetilde{L}^s \equiv \widetilde{L}(\mathbf{x}^s, M_{200})$. For a detailed derivation of equations (8)–(10), please see Appendix A.

In practice, we actually determine the logarithm of the mass, $\log_{10}(M_{200})$, since the resulting probability distribution function (PDF) in log space is closer to a Gaussian. We determine the most likely host mass as the mass that maximizes the likelihood – the Maximum Likelihood Estimator (MLE) mass, M_{200}^{MLE}. As the uncertainties, we take the 68 per cent confidence limits corresponding to the interval between the 16 and 84 percentiles of the mass PDF. Assuming that the satellites are independent tracers, we can combine the estimates for individual satellites to obtain an overall estimate, given a set of observations, $\{\mathbf{x}^s\}$. The combined likelihood is given by

$$p\left(M_{200}|\{\mathbf{x}^s\}\right) = \prod_{s=1}^{N_{\mathrm{Sat}}} p\left(M_{200}|\mathbf{x}^s\right) . \qquad (11)$$

The potential energy of satellites has a weak dependence on the host halo concentration, which is an unknown quantity. We have tested that the 10 satellites used here cannot, by themselves, place any meaningful constraints on the concentration of the MW halo. Thus, we proceed to marginalize over the unknown concentration:

$$p\left(M_{200}|\mathbf{x}^s\right) = \int p\left(M_{200}|\mathbf{x}^s, C\right) p\left(C|M_{200}\right) \mathrm{d}C , \qquad (12)$$

where $p(C|M_{200})$ denotes the distribution of concentrations for haloes of mass, M_{200}, found in the EAGLE simulation, which we took from Schaller et al. (2015). In practice, we evaluate $p(M_{200}|\mathbf{x}, C)$, using 15 evenly spaced values in the range $C \in [5, 20]$. We note that the dependence on concentration is weak, so our results are not affected by the choice of the distribution of concentrations (see Appendix C)

3.1 Observational errors

While we have perfect knowledge of the phase space coordinates, $\{\mathbf{x}^s\}$, of EAGLE satellites, in order to apply the method to the MW satellites, we must consider the effects of observational errors. To account for errors, we perform a set of 1000 Monte Carlo realizations that sample the observational uncertainties (see Section 2.2 for a detailed description of the procedure). This produces a Monte Carlo sample of allowed phase-space coordinates for each satellite. We first determine the MW mass likelihood for each Monte Carlo realization, and then we average the likelihood of all the Monte Carlo samples. In the limit of a large number of Monte Carlo samples, this is equivalent to marginalizing over the observational errors.
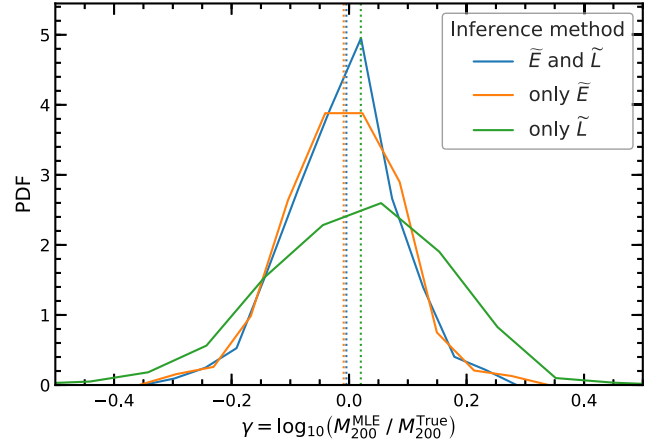

Figure 3. The distributions of the ratio of MLE estimate, M_{200}^{MLE}, to the true halo mass M_{200}^{True}, from each of our three inference methods. The results were obtained by applying each mass determination method to a sample of $\sim$600 systems from the EAGLE simulation. The vertical dotted lines indicate the median of each distribution, which represents the bias, b, of each method. For subsequent results, we correct the mass estimates by the bias of each method and we denote the corresponding mass by M_{200}^{Esti}.

3.2 Method calibration using EAGLE

To provide a robust mass estimate of the MW halo, we now explore the accuracy of our methods using tests on mock satellite systems. Since MLE estimates can be biased, we first calibrate the inference methods using a large sample of EAGLE systems. Then, in Section 3.3, we validate the methods on an independent, higher resolution set of simulations taken from the AURIGA project.

To calibrate the three mass determination methods, we start by applying them to the EAGLE simulations. We select the same EAGLE haloes as in Section 2.3, that is haloes of total mass $\sim 10^{12}$ M$_\odot$, and keep only those that contain at least 10 luminous satellites within the distance range quoted in Section 2.3. There are $\sim$600 haloes satisfying the selection criteria. We then apply each mass determination method to each EAGLE system to obtain the MLE mass, M_{200}^{MLE} of that system. The results are shown in Fig. 3, where we compare the MLE masses to the true total halo mass, M_{200}^{True}. The performance of each method may be quantified by the ratio, $\gamma = \log_{10}\left(M_{200}^{\mathrm{MLE}}/M_{200}^{\mathrm{True}}\right)$, for each EAGLE system. The median and scatter of the γ distribution give the bias and typical uncertainty of the method, respectively.

Fig. 3 shows that our three methods have only small biases compared to their dispersion. The (E, L) and the E only methods have a slight bias with the median of the γ distribution being -0.01, while the method based on L only has a bias of $+0.02$. A consistently biased estimate is not a problem since it can easily be corrected to obtain an accurate result. The bias-corrected mass estimate, M_{200}^{Esti}, is given by

$$\log_{10}\left(M_{200}^{\mathrm{Esti}}\right) = \log_{10}\left(M_{200}^{\mathrm{MLE}}\right) - b. \qquad (13)$$

The dispersion of the γ distributions in Fig. 3 reflects the true precision of the method, σ_{True}. Mass estimates based only on the angular momentum have the largest dispersion, $\sigma_{\mathrm{True}} = 0.15$, while both E and (E, L) methods have the same precision, $\sigma_{\mathrm{True}} = 0.09$. Thus, most of the mass information is contained in the satellites' orbital energy. Adding angular momentum data hardly improves the mass estimates, indicating that L does not contain significant
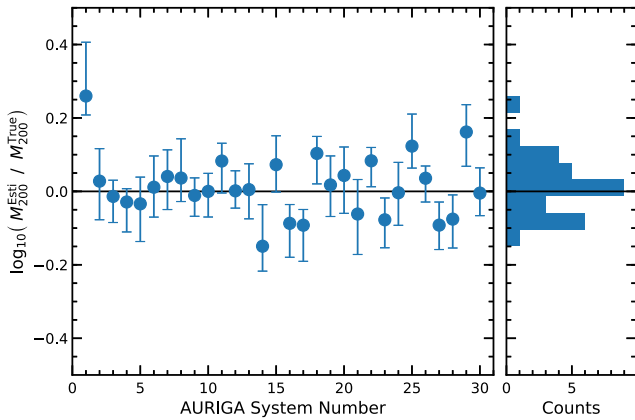
Figure 4. Test of the energy–angular momentum halo mass inference method on 30 MW-mass galaxies from the AURIGA galaxy formation simulation project. We show the ratio between the estimated, $M_{200}^{\rm Esti}$, and the true, $M_{200}^{\rm True}$, halo masses for each AURIGA system. Note that $M_{200}^{\rm Esti}$ includes the bias correction determined from the EAGLE mock catalogues (see equation 13). The error bars correspond to the estimated 68 per cent confidence limit. The AURIGA simulations have much higher resolution and assume different galaxy formation models than EAGLE, and thus provide a rigorous test of the mass inference method. Most mass estimates agree with the true values within the 68 per cent confidence limit, in very good agreement with statistical expectations.

information about the host mass beyond the information already contained in the satellites' energy.

Another important point to consider is the confidence interval to be associated with each mass measurement. One possibility is to take the dispersion of γ (see Fig. 3), but this suffers from the limitation of assigning the same error to all mass measurements. In practice, the mass of some host haloes can be more precisely determined than the mass of others, and the confidence limits do not need to be symmetrical around the MLE value (e.g. see Fig. 4). Thus, the approach of assigning a single error to all measurements is not optimal.

An alternative is to consider the error estimates of the Bayesian method. These should be accurate, except for the effects of an assumption implicit in our method, that all satellites are independent tracers. For example, satellites can fall in groups or filaments, which might result in correlated energy and angular momentum amongst two or more satellite galaxies. For the brightest 10 satellites, the ones considered here, only a small fraction is expected to have fallen in groups (e.g. Wetzel, Deason & Garrison-Kimmel 2015; Shao et al. 2018b) and, in any case, interactions with other satellites and with the host halo and galaxy are expected to decrease any phase-space correlations present at the time of accretion (e.g. Deason et al. 2015; Shao, Cautun & Frenk). Thus, we would generally expect the assumption of independent tracers to be reasonable. We have checked how realistic the Bayesian error estimates are and found them to be roughly the same as the uncertainties shown in Fig. 3. The same will not hold true in future studies when the method will be applied to much larger numbers of satellites (see discussion in Section 4.3).

3.3 Tests with the AURIGA simulations

In this section we test our mass inference methods by applying them to model galaxies from the AURIGA project. AURIGA is a suite of high-resolution, hydrodynamical zoom-in simulations of MW-
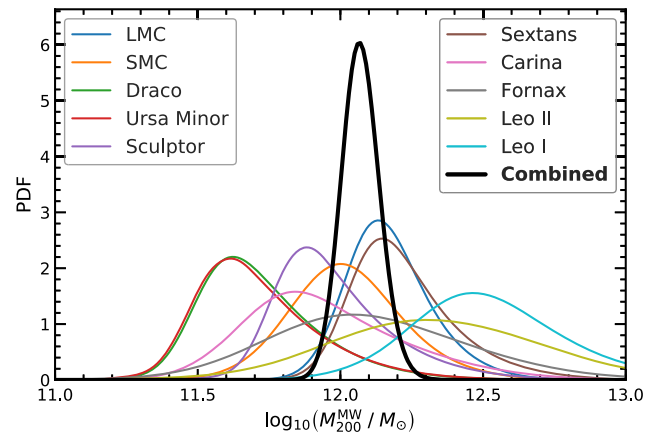

Figure 5. The MW halo mass, $M_{200}^{\rm MW}$, inferred from the energy and orbital angular momentum of each classical satellite (except *Sagittarius*). The thick line shows the inferred MW halo mass, $M_{200}^{\rm MW} = 1.04_{-0.14}^{+0.23} \times 10^{12}\,{\rm M_\odot}$ (68 per cent confidence limit), obtained by combining the 10 individual estimates. The inferred $M_{200}^{\rm MW}$ values and their corresponding errors are given in Table 2.

like systems. We consider the 30 level 4 systems, which have DM and gas mass resolution $\sim$30 times higher than EAGLE (see Grand et al. 2017 for details). AURIGA makes for a perfect test suite since it has higher resolution, uses a different hydrodynamics code, and includes a different galaxy formation model than EAGLE. Thus, by applying our inference methods to these completely independent simulations, we can assess our methods' accuracy and quantify any systematic biases that may have been introduced by calibrating our methods on the EAGLE simulations.

For each AURIGA galaxy, we identify the brightest 10 satellites galaxies at a distance between 40 and 300 kpc from the halo centre. These objects represent our mock observational sample of the MW-like satellite systems. We then apply the (E, L) mass determination method to each of the 30 AURIGA systems.

Fig. 4 shows the ratio of estimated to true masses, as well as the associated uncertainties for each AURIGA galaxy. We find that for 19 out of the 30 systems, or 63 per cent, the estimated mass agrees with the true value to the 68 per cent confidence interval, approximately as expected from the statistics. This performance is very good especially when taking into account that around a third of the AURIGA systems are unrelaxed (see Section 2.3 for relaxation criteria). We have checked that the other two methods, using only L and only E, are similarly successful. This test demonstrates the accuracy of our method for determining halo masses and confirms that our error estimates are realistic and robust.

4 MILKY WAY MASS ESTIMATES

We now apply our mass estimation methods to data for the 10 MW satellites that satisfy our selection criteria. We begin by obtaining the Galactic halo mass likelihood from each satellite and corresponding uncertainties (calculated with the Monte Carlo sampling technique described in Section 3.1). The PDFs of the MW halo mass, M_{200}, obtained from each satellite's data using the (E, L) method are shown in Fig. 5; the best estimates and associated 68 per cent confidence intervals are given in Table 2.

Individually, the satellites give a wide range of total masses for the MW. For example, *Ursa Minor* and *Draco* favour a very low mass, $M_{200} \approx 10^{11.6}\,{\rm M_\odot}$, which is because both of them have very low

Table 2. The MW halo mass, M_{200}^{MW} (the mass enclosed within a sphere of average density 200 times the critical density) estimated from each classical satellite (except *Sagittarius*), and the combined overall result. The table gives mass estimates using (i) only the angular momentum, L; (ii) only the energy, E; and (iii) both E and L. We quote 68% confidence limits.

| Satellite	M_{200}^{MW} [10^{12} M$_\odot$]		
	only L	only E	E and L
LMC	$0.98^{+1.78}_{-0.51}$	$1.23^{+0.65}_{-0.25}$	$1.35^{+0.76}_{-0.28}$
SMC	$0.98^{+1.84}_{-0.52}$	$0.93^{+0.61}_{-0.31}$	$1.00^{+0.68}_{-0.32}$
Draco	$0.51^{+0.94}_{-0.26}$	$0.4^{+0.39}_{-0.09}$	$0.42^{+0.43}_{-0.08}$
Ursa Minor	$0.56^{+1.03}_{-0.32}$	$0.40^{+0.40}_{-0.09}$	$0.42^{+0.43}_{-0.09}$
Sculptor	$1.02^{+1.88}_{-0.52}$	$0.74^{+0.66}_{-0.15}$	$0.76^{+0.74}_{-0.14}$
Sextans	$1.70^{+3.09}_{-0.87}$	$1.35^{+1.01}_{-0.29}$	$1.41^{+1.12}_{-0.28}$
Carina	$1.29^{+2.34}_{-0.69}$	$0.74^{+0.83}_{-0.24}$	$0.69^{+1.02}_{-0.21}$
Fornax	$1.86^{+3.63}_{-1.08}$	$1.12^{+1.68}_{-0.52}$	$1.10^{+1.78}_{-0.52}$
Leo II	$3.02^{+5.63}_{-1.86}$	$1.91^{+4.32}_{-1.01}$	$2.04^{+3.17}_{-1.11}$
Leo I	$2.40^{+4.61}_{-1.49}$	$3.09^{+6.45}_{-1.16}$	$2.88^{+3.43}_{-1.06}$
Combined	$\mathbf{1.20^{+0.42}_{-0.27}}$	$\mathbf{1.10^{+0.21}_{-0.14}}$	$\mathbf{1.17^{+0.21}_{-0.15}}$
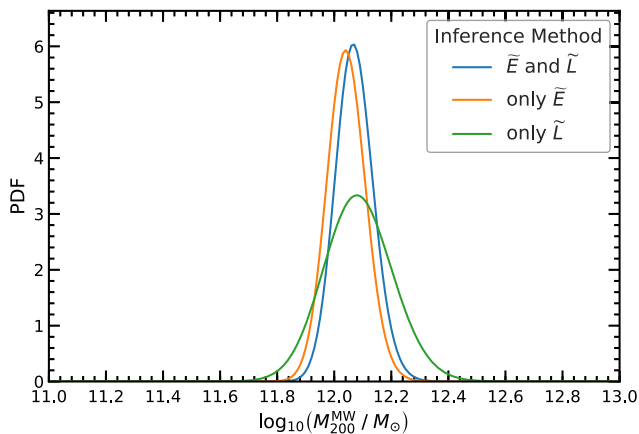
Figure 6. Comparison of the MW halo mass inferred using the three methods studied here. The methods use the following satellite data: (i) only the angular momentum, L; (ii) only the energy, E; and (iii) both E and L. The mass estimates and their errors are given in Table 2.

total specific energies (see Table 1). At the other extreme, *Leo I* has the highest total energy and favours a halo an order of magnitude more massive, $M_{200} \approx 10^{12.5}$ M$_\odot$. However, the mass estimate from any one satellite has a broad distribution and does not provide a strong constraint on the MW mass. The true power of the method comes from combining the mass likelihoods from each satellite; the combined result is shown as a thick line in Fig 5. The combined estimate for the MW halo mass is $M_{200}^{MW} = 1.17^{+0.21}_{-0.15} \times 10^{12}$ M$_\odot$.

Fig. 6 compares the Galactic halo mass determination using the three methods introduced in this study. We find very good agreement amongst the three, with all of them having a very large overlap (see Table 2 for the actual values and their uncertainties). Of the three, the method based on angular momentum only is the most uncertain and, of the remaining two, the one based on energy only gives a slightly lower uncertainty. As we saw in Fig. 3, adding L data to E data does not produce an improvement in the mass determination, which is what we find here too. In fact, the (E, L) method seems to have slightly larger uncertainties than the E-only method; however, the difference is very small and not statistically significant. We also

find that the estimated uncertainties in the MW mass determination are similar to the ones shown in Fig. 3, where we tested the methods on the EAGLE simulations. As we will see in Figs 10 and 11, the uncertainties in the mass are dominated by the small number of satellites, not by their proper motion errors.

It is important to consider possible systematics that may affect our mass determination. For example, the *LMC* and *SMC* are believed to have fallen in recently as a pair (e.g. Kallivayalil et al. 2013), and might not encode independent information about the MW halo. We have checked that discarding the *SMC* from our analysis does not significantly change the median estimate and leads only to a small increase in the uncertainty range. We also know that the classical satellites are atypical in at least two respects: they currently reside in a thin plane, with several orbiting preferentially within it, and they have a very low-velocity anisotropy. These two properties place the MW satellite system in the tail of the ΛCDM expectations (e.g. see Pawlowski et al. 2014; Cautun et al. 2015; Cautun & Frenk 2017). The analysis described in Appendix D shows that the distribution of E and L values of the Galactic satellites is, in fact, consistent with ΛCDM predictions, with no evidence for any tension.

4.1 Comparison to previous MW mass estimates

In Fig. 7 we compare our total MW halo mass estimate with a selection of results from previous studies. This figure is an update of fig. 1 in Wang et al. (2015) and includes recent estimates, especially those that use *Gaia* DR2 data. Some mass determination methods, such as ours and those based on Local Group dynamics (e.g. Li & White 2008; Peñarrubia et al. 2016) and satellite dynamics (e.g. Watkins et al. 2010; Boylan-Kolchin et al. 2013; Barber et al. 2014; Eadie, Harris & Widrow 2015), give the total mass directly, but many others, such as those using globular clusters (e.g. Posti & Helmi 2018; Watkins et al. 2018) or halo stars (e.g. Xue et al. 2008; Gnedin et al. 2010; Deason et al. 2012; Huang et al. 2016), give the enclosed mass only within an inner region of the MW halo and require an assumption about the MW halo mass profile for extrapolation to the total mass. Despite the wide range of values quoted in the literature, our result is consistent within 1σ with the majority of previous mass estimates. Our errors are significantly smaller than those of most previous estimates and, most importantly, we have rigorously and extensively tested our method on simulated galaxies to produce an accurate, unbiased mass estimate with realistic uncertainties.

Our estimated value of $\sim 10^{12}$ M$_\odot$ for the MW halo mass has important implications for the interpretation of the satellite population of our galaxy, which is often used as a testbed for the ΛCDM model. For example, the 'too-big-to-fail' problem (Boylan-Kolchin et al. 2011), which refers to the number of massive, dense satellites in the MW halo, is significantly alleviated. Indeed, Wang et al. (2012) showed that approximately 40 per cent of haloes with mass $M_{halo} \sim 10^{12}$ M$_\odot$ in ΛCDM only simulations have three or fewer subhaloes with $V_{max} > 30$ km s^{-1} (the threshold used by Boylan-Kolchin et al. 2011 to define massive failures). For the MW halo mass that we infer, the 'too-big-to-fail problem' is not a failure of ΛCDM.

An accurate estimate of the MW halo mass is also crucial to address properly the missing satellites problem. The total number of subhaloes depends strongly on the halo mass (doubling the halo mass, roughly doubles the number of subhaloes). Thus, when appealing to baryonic physics solutions to this problem, such as the influence of reionization and stellar feedback, an accurate estimate of the halo mass is a pre-requisite for a realistic model. Moreover, when the halo mass is known, the number of subhaloes may even
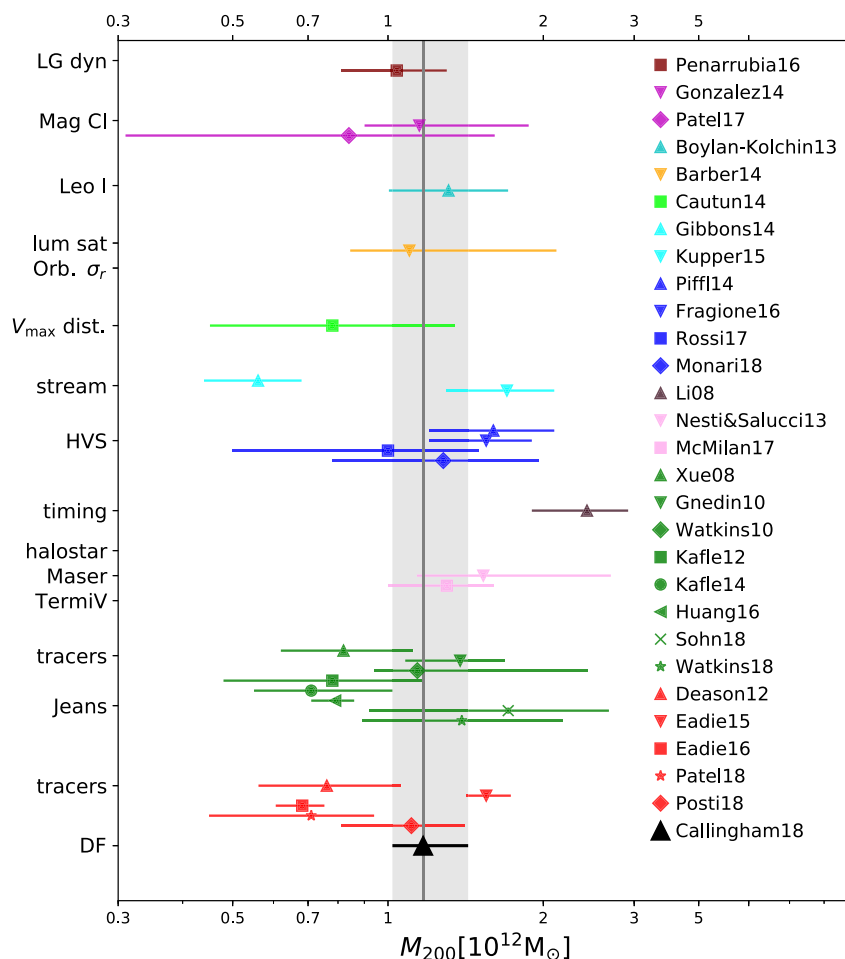
Figure 7. Comparison of our inferred MW halo mass with a selection of previous estimates. The vertical line and the shaded region show our M_{200} estimate and its 68 per cent confidence limit. The remaining symbols show previous estimates (see the legend), with the horizontal lines corresponding to the quoted 68 per cent confidence limits. The results are grouped according to the methodology employed (see the vertical axis). We give the mass, M_{200}, contained within R_{200} (the radius enclosing a mean density equal to 200 times the critical density). Some of the previous estimates were converted to M_{200} by assuming an NFW profile and the mean concentration predicted for that mass.

inform us about these critical processes, such as when the epoch of reionization occured (see e.g. fig. 1 in Bose, Deason & Frenk 2018), or indeed about the identity of the DM (Kennedy et al. 2014; Lovell et al. 2014).

4.2 The concentration of the MW halo

Alongside mass, the other fundamental property of DM haloes is their concentration. Besides being one of the key parameters of the NFW profile, the concentration encodes crucial information about the halo's formation history (e.g. Wechsler et al. 2002; Lu et al. 2006; Ludlow et al. 2014) and, after halo mass, is the most important property for determining how galaxies populate haloes (e.g. Matthee et al. 2017). Our MW halo mass estimate does not depend on, or constrain, the MW halo concentration. However, when combined with mass estimates for the inner regions of the Galaxy, we can use our mass estimate to infer the concentration of the MW halo. For this, we use inner mass determinations based on the dynamics of the globular cluster population. This population is much more radially concentrated than the satellite galaxy population, and there are a large number of globular clusters with precise *Gaia* DR2 proper motion measurements (Gaia Collaboration 2018a). This enabled

Posti & Helmi (2018) and Watkins et al. (2018) to estimate the total mass enclosed within ∼20 kpc from the Galactic Centre with high precision.

To determine the concentration, we assume that the DM distribution follows the NFW profile, which provides a very good fit to the DM density profiles in both DM-only and hydrodynamic simulations. To determine the enclosed DM mass, we subtract the MW baryonic mass, $M_{MW}^{baryons}$, from the total mass measurements within both 20 kpc and R_{200}. We use the McMillan (2017) estimates: a stellar mass of 5.4×10^{10} M$_\odot$ and a gas mass of 1.2×10^{10} M$_\odot$, which corresponds to $M_{MW}^{baryons} = 6.6 \times 10^{10}$ M$_\odot$.

Fig. 8 shows the fraction of DM mass enclosed within 20 kpc of the centre as a function of the halo concentration; the solid lines and shaded regions indicate the inferred concentrations and their 68 per cent confidence ranges. The Posti & Helmi (2018) estimate gives a mass ratio, $M^{DM}(< 20\,\mathrm{kpc})/M_{200}^{DM} \approx 0.12$, which corresponds to a concentration of $C = 10.9_{-2.0}^{+2.6}$ (68 per cent confidence limits), where the errors were calculated by Monte Carlo sampling of the uncertainties associated with the inner and total mass estimates. The same analysis for the Watkins et al. (2018) inner mass estimate gives $M^{DM}(< 21.1\,\mathrm{kpc})/M_{200}^{DM} \approx 0.20$, and a concentration, $C = 11.8_{-3.8}^{+5.1}$. To include the Watkins et al. result
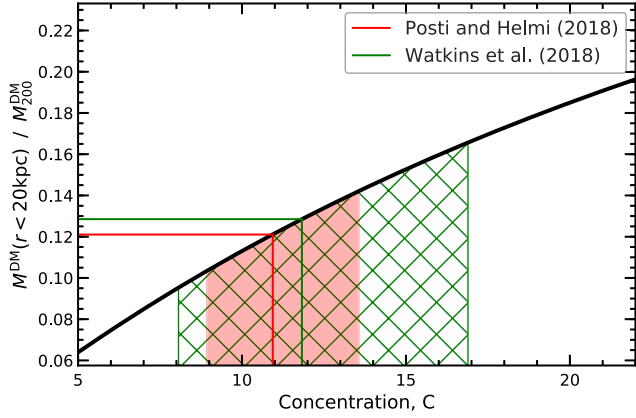
Figure 8. The concentration of the MW halo inferred by combining our total mass estimate with previous inner mass estimates. The solid thick curve shows the DM mass fraction, $M^{DM}(< 20\ \mathrm{kpc})/\mathrm{M}_{200}^{DM}$, contained within 20 kpc of the halo centre as a function of concentration, C, for our best estimate of a total halo mass of $M_{200}^{DM} = 1.11 \times 10^{12}\ \mathrm{M}_\odot$. The two horizontal lines correspond to the Posti & Helmi (2018) and Watkins et al. (2018) inner mass estimates. The inferred concentrations are shown by the two vertical lines, with the shaded regions corresponding to the 68 per cent confidence ranges. We find $C = 10.9^{+2.6}_{-2.0}$ and $C = 11.8^{+5.1}_{-3.8}$ for the Posti & Helmi and Watkins et al. inner mass estimates, respectively.

in Fig. 8, we rescaled their mass estimate to a fiducial distance of 20 kpc.

We find that the MW halo has a high concentration for its mass, with a most likely value of $C \sim 10.9$, which could suggest that the MW halo assembled early. The high MW halo concentration is supported by other studies; for example, the best-fitting Galaxy model of McMillan (2017) gives $C = 16 \pm 3$. In the EAGLE simulations, the median concentration of an $\sim 10^{12}\ \mathrm{M}_\odot$ halo is ~ 8.2 and only ~ 23 per cent of haloes have a concentration higher than 10.9, which suggests that the MW halo is an outlier.

However, the presence of central baryonic components causes a contraction of the very inner region of $\sim 10^{12}\ \mathrm{M}_\odot$ mass haloes, increasing the total mass in the inner region. As a result, the inner region is not well described by an NFW profile, and the inferred concentration is biased high (e.g. Schaller et al. 2015). To overcome this limitation, in Fig. 9 we compare the inner DM mass fraction of the MW to that of similar mass haloes in the EAGLE and AURIGA simulations and find that the MW is typical of haloes in both simulations. The systematic difference between the EAGLE and AURIGA distribution reflects the stellar mass content of those objects: compared to abundance matching results, galactic mass haloes in EAGLE have stellar masses that are too low, while equal mass haloes in AURIGA have stellar masses that are too high.

4.3 Improving the mass estimate

In this section we discuss the limitations of our method and ways of improving the MW mass estimate. There are two main sources of uncertainty: statistical, from the finite number of satellites, and systematic, from halo-to-halo variation. The former can be reduced by increasing the number of dynamical tracers and/or reducing observational errors, but the latter cannot be reduced.

We begin by investigating the effect of observational errors on the MW halo mass determination. The main source of observational uncertainties is the proper motion measurements. As such, we consider the effect of varying the errors, $\sigma_{\mu_\alpha}^s$ and $\sigma_{\mu_\delta}^s$, associated with
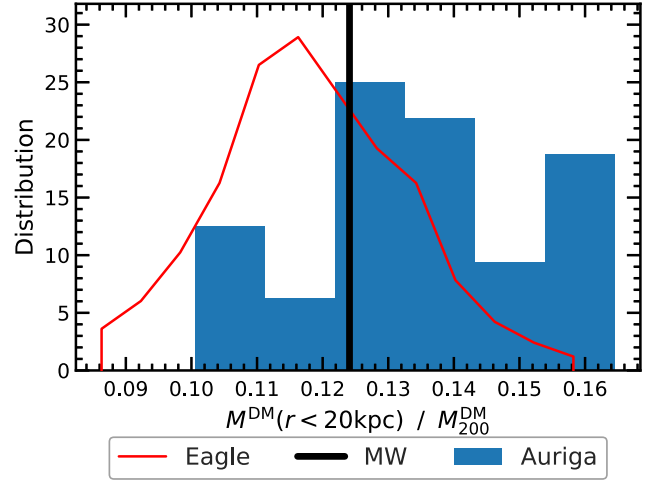
Figure 9. The distribution of the DM mass fraction contained within 20 kpc of the halo centre, $M^{DM}(< 20\ \mathrm{kpc})/\mathrm{M}_{200}^{DM}$, for MW-sized galaxies in EAGLE and AURIGA. The red line shows the distribution of systems from our EAGLE sample described in Section 2.3, whose M_{200} is within 0.2 dex of our MW mass estimate. The blue histogram gives the distribution of the 30 level 4 AURIGA systems described in Section 3.3. The thick black line shows the MW's DM mass fraction; calculated using our own MW halo mass estimate, M_{200}^{DM} and $M^{DM}(< 20\ \mathrm{kpc})$, from Posti & Helmi (2018).
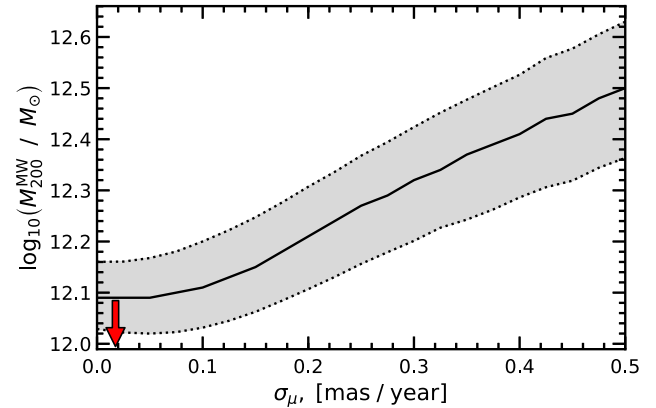

Figure 10. The estimated MW halo mass, M_{200}^{MW}, as a function of the size of proper motion errors, σ_μ. Results are shown only for the inference method based on both $\widetilde{E}$ and $\widetilde{L}$ values. The solid line gives the mass estimate, while the shaded region shows the 68 per cent confidence interval. Larger values of σ_μ result in more uncertain mass estimates and also in a systematic bias with respect to the true mass. The red arrow shows the median error for our sample of classical satellites.

the two components of the proper motion. For the MW observations these errors vary from satellite to satellite, from 0.005 mas yr^{-1} for *Sculptor* to 0.039 mas yr^{-1} for *Leo II*, with a median of ~ 0.018 mas yr^{-1}. For simplicity, here we assume the same error for all satellites, that is $\sigma_{\mu_\alpha}^s = \sigma_{\mu_\delta}^s = \sigma_\mu$, and study the effect of observational errors by varying σ_μ. For each σ_μ value, we proceed by taking the current proper motions of each MW satellite and resetting their errors to the target value of σ_μ. Then, we generate a sample of Monte Carlo realizations, using the procedure described in Section 2.2 and apply the mass estimation method.

Fig. 10 shows the MW halo mass estimate inferred from the (E, L) method as a function of the size of the proper motion errors, σ_μ. As we increase σ_μ, we find, as expected, that the uncertainty in the

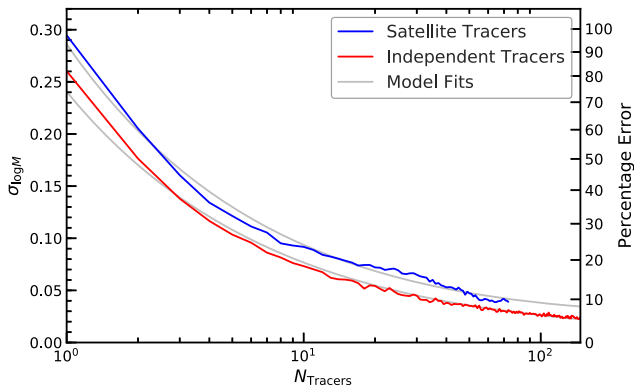**Figure 11.** The 1σ uncertainty, $\sigma_{\log_{10} M}$, with which we can determine the logarithm of the halo mass as a function of the number of satellite galaxy tracers, N_{tracers}, included in the sample. We show the mean uncertainty for a large number of EAGLE haloes whose mass was determined using the E and L values of their most massive N_{tracers} satellites. The right-hand axis shows the percentage errors in M_{200} corresponding to the $\sigma_{\log_{10} M}$ values. The blue line gives the results using the satellites of EAGLE galaxies. The red line gives the results from idealized cases of independent satellite tracers (see the main text) and represents the statistical limit of our method. The two grey lines show the best-fitting curves using equation (14).

mass determination increases. However, the current proper motion errors for the classical satellites are so small that they fall in the region where there is hardly any dependence of the mass estimate on σ_μ. Improving the current observational errors will provide little improvement on the mass estimate.

More importantly, we also find a systematic shift in the estimated halo mass, which increases rapidly with the size of the proper motion errors. For example, for $\sigma_\mu \approx 0.35$ mas yr^{-1}, the estimated mass is a factor of 2 too high. This comes about because large proper motion errors bias the observed velocities high, thus leading to higher energy and angular momentum values, which, in turn, lead to higher mass estimates. This is not a problem for our current estimate since all the classical satellites have proper motions errors well below 0.1 mas yr^{-1}, and thus lie in the region where the mass estimate is flat. However, were we to include in the sample ultrafaint dwarf satellites, many of which have large proper motion errors (e.g. Fritz et al. 2018), then we would need to account for the additional bias introduced by the observational errors.

The MW is predicted to have approximately 125 satellites brighter than $M_V = 0$, of which just over 50 have already been discovered (Newton et al. 2018). This means that, in principle, many more satellites can be used to determine the MW halo mass, potentially with a smaller uncertainty. Fig. 11 quantifies how the uncertainty in halo mass is reduced as the number of satellite galaxies in the sample increases. Here, we consider the simplified case where there are no observational errors and focus only on the variation arising from the number of tracers, N_{Tracers}.

Using the same sample of EAGLE main haloes as in Section 2.3, we determine the host halo mass using the most massive N_{Tracers} subhaloes. To obtain large enough tracer counts in EAGLE, we relax the criteria and consider not only luminous satellites, but also dark subhaloes. Many of these would be the hosts of the ultrafaint dwarfs, but EAGLE lacks the resolution to populate them with stars. However, these dark substructures are well resolved and their orbital properties are reliable. To estimate an average error for each value of N_{Tracers}, we calculate the dispersion in the distribution of $\log_{10}(M_{200}^{\text{Esti}}/M_{200}^{\text{True}})$: the logarithm of the ratio of estimated to true

mass. To ensure accurate measures of the average error, we require at least 100 systems that have N_{Tracers} or more tracers; this limits our analysis to $N_{\text{tracers}} \leq 72$.

The blue line in Fig. 11 shows that the expected error in our mass estimate, $\sigma_{\log_{10} M}$, decreases as the number of tracers increases. We would expect that above a certain number of tracers, the mass determination does not improve any more because the error becomes dominated by halo-to-halo variation and systematic effects such as correlations between the kinematics of different satellites (see e.g. Wang et al. 2017, 2018).

To investigate these effects, we construct idealized systems by selecting N_{Tracers} satellites from our samples' DF, $F(\widetilde{E}, \widetilde{L})$, and then scale them to the mass of random host haloes selected from our sample. This gives us a population of systems whose satellites are perfectly described as being independently drawn from our distribution. As an additional advantage, we are not limited to $N_{\text{Tracers}} \leq 72$, and can continue increasing N_{Tracers} as $\sigma_{\log_{10} M}$ asymptotes to zero (Fig. 11, red line). The difference between the errors in the two samples is the error due to halo-to-halo scatter, σ_{Scatter}. The dependence of the total error, $\sigma_{\log_{10} M}$, on N_{Tracers} can be modelled as (cf. Li et al. 2017):

$$\sigma_{\log_{10} M}^2 = \frac{\sigma_{\text{Stat}}^2}{N_{\text{Tracers}}} + \sigma_{\text{Scatter}}^2 \ . \tag{14}$$

The mass error for the true EAGLE satellite systems is best fitted by $\sigma_{\text{Stat}} = 0.29$ and $\sigma_{\text{Scatter}} = 0.03$, while the error for the idealized systems of independent tracers is best described by $\sigma_{\text{Stat}} = 0.24$ and $\sigma_{\text{Scatter}} = 0.01$. We note that a scatter error, $\sigma_{\text{Scatter}} = 0.03$, equates to an accuracy limit of around 5 per cent and would represent the best mass measurement of the method in the limit of a very large number of tracers. For 10 satellite tracers we obtain an $\sim$20 per cent uncertainty, similar to our MW mass estimate, while the idealized mass estimates give a slightly smaller uncertainty of $\sim$16 per cent. The fits suggest that an $\sim$10 per cent determination of the MW mass is achievable by applying our method to around $N_{\text{tracers}} \approx 60$ tracers. The accuracy of our halo mass measurement could be further improved by considering the dependence of the satellite dynamics on the properties and assembly history of the host halo. It is conceivable that by restricting the analysis to a subset of haloes that more closely resembles the MW, such as haloes with a similar assembly history, the halo-to-halo variation could be reduced, leading to an even more precise halo mass determination. However, at present, the largest benefit would accrue from increasing the number of tracers.

5 CONCLUSIONS

We have developed a method to determine the total mass of the MW DM halo by comparing the energy and angular momentum of MW satellites with the respective distributions predicted in the EAGLE galaxy formation cosmological simulations. When scaled appropriately by host halo mass, the energy and angular momentum of the satellites become independent of the host halo mass (see Fig. B1). Thus, we can use a large sample of EAGLE haloes, and associated satellites, in our estimate of the MW halo mass. For this, we constructed the satellite DF in (E, L) space from the simulations and carried out a maximum likelihood analysis to infer the halo mass from the phase-space properties of the 10 brightest satellite galaxies (excluding the disrupting *Sagittarius* galaxy). Using mock samples from EAGLE, we analysed the performance of the method and quantified its statistical and systematic uncertainties.

A key test of our method was to apply it to estimate the masses of the DM haloes of 30 MW analogues simulated in the AURIGA project. These simulations have much higher resolution and employ different baryonic physics models than EAGLE. They produce realistic MW-like galaxies (Grand et al. 2017, 2018) and thus provide a rigorous and completely independent external test of our method. We find that our method provides an unbiased estimate of the total halo masses of the AURIGA galaxies, with a precision of ~16 per cent, in very good agreement with the expectations from the EAGLE simulations.

Our main conclusions are as follows:

(i) Applying our method to 10 classical MW satellites gives an estimate for the total mass of the MW halo of $M_{200}^{\mathrm{MW}} = 1.17^{+0.21}_{-0.15} \times 10^{12}\,\mathrm{M}_\odot$. This result agrees well with most previous estimates in the literature but with a rigorously tested accuracy (~15 per cent), which is better than most other estimates.

(ii) Combining our total DM halo mass estimate with recent estimates of the halo mass within 20 kpc gives an inner DM mass fraction, $M^{\mathrm{DM}}(< 20\,\mathrm{kpc})/M_{200}^{\mathrm{DM}} \approx 0.12$. Assuming that the MW halo follows an NFW profile, we have inferred a Galactic concentration, $C = 10.9^{+2.6}_{-2.0}$. This is higher than typical EAGLE haloes with masses of $10^{12}\,\mathrm{M}_\odot$, which have a median concentration of 8.2, with only ~23 per cent of them having concentrations of 10.9 or higher. The discrepancy likely reflects that an NFW profile is not a good description of the inner region since the Galactic halo has contracted due to the baryonic components. In fact, when comparing the inner DM mass fraction of the MW against the EAGLE and AURIGA simulations, our galaxy is typical of similar mass haloes.

(iii) Our halo mass estimate can be improved by increasing the number of halo tracers and/or reducing the observational uncertainties. We found that the observed proper motions of the 10 classical satellites are already so precise that further improvement will make little difference to the halo mass estimate. Increasing the number of satellites, on the other hand, for example by including the ~50 currently known satellites in the MW, would reduce the mass errors to ~11 per cent. Further improvements would be possible by analysing all ~125 satellites that are predicted to reside in the MW (Newton et al. 2018), which would result in an ~8 per cent mass uncertainty, a factor of 2 improvement over our current estimate.

In summary, our MW halo mass estimate is precise and accurate and has been thoroughly tested on realistic model galaxies and their satellite populations. Mass estimates that rely on cosmological simulations are relatively new, but the use of simulations enables a robust and testable methodology. Indeed, the accuracy we are now able to achieve (~15 − 20 per cent; see also Patel et al. 2018) is a significant step forward from the factor of 2 uncertainty that has plagued MW mass estimates for years. This theoretical boost, coupled with the exquisite six-dimensional data that *Gaia* and complementary facilities are now providing, brings us closer to what may be called the era of 'precision' near-field cosmology – when we can go beyond rough estimates of the MW halo mass and, instead, remove this important degree of freedom when making use of the properties of the MW to inform cosmological models and DM theories.

REFERENCES

Barber C., Starkenburg E., Navarro J. F., McConnachie A. W., Fattahi A., 2014, MNRAS, 437, 959
Binney J., Wong L. K., 2017, MNRAS, 467, 2446
Bose S., Deason A. J., Frenk C. S., 2018, ApJ, 863, 123
Bowden A., Belokurov V., Evans N. W., 2015, MNRAS, 449, 1391
Bower R. G., Schaye J., Frenk C. S., Theuns T., Schaller M., Crain R. A., McAlpine S., 2017, MNRAS, 465, 32
Boylan-Kolchin M., Bullock J. S., Kaplinghat M., 2011, MNRAS, 415, L40
Boylan-Kolchin M., Bullock J. S., Sohn S. T., Besla G., van der Marel R. P., 2013, ApJ, 768, 140
Busha M. T., Marshall P. J., Wechsler R. H., Klypin A., Primack J., 2011a, ApJ, 743, 40
Busha M. T., Wechsler R. H., Behroozi P. S., Gerke B. F., Klypin A. A., Primack J. R., 2011b, ApJ, 743, 117
Cautun M., Frenk C. S., 2017, MNRAS, 468, L41
Cautun M., Hellwing W. A., van de Weygaert R., Frenk C. S., Jones B. J. T., Sawala T., 2014a, MNRAS, 445, 1820
Cautun M., Frenk C. S., van de Weygaert R., Hellwing W. A., Jones B. J. T., 2014b, MNRAS, 445, 2049
Cautun M., Bose S., Frenk C. S., Guo Q., Han J., Hellwing W. A., Sawala T., Wang W., 2015, MNRAS, 452, 3838
Cole D. R., Binney J., 2017, MNRAS, 465, 798
Crain R. A. et al., 2015, MNRAS, 450, 1937
Deason A. J., Belokurov V., Evans N. W., An J., 2012, MNRAS, 424, L44
Deason A. J., Wetzel A. R., Garrison-Kimmel S., Belokurov V., 2015, MNRAS, 453, 3568
Eadie G. M., Harris W. E., 2016, ApJ, 829, 108
Eadie G. M., Harris W. E., Widrow L. M., 2015, ApJ, 806, 54
Evans N. W., Wilkinson M. I., Perrett K. M., Bridges T. J., 2003, ApJ, 583, 752
Fragione G., Loeb A., 2017, New A, 55, 32
Fritz T. K., Battaglia G., Pawlowski M. S., Kallivayalil N., van der Marel R., Sohn S. T., Brook C., Besla G., 2018, A&A, 619, A103
Gaia Collaboration, 2018a, A&A, 616, A1
Gaia Collaboration, 2018b, A&A, 616, A12
Gibbons S. L. J., Belokurov V., Evans N. W., 2014, MNRAS, 445, 3788
Gnedin O. Y., Kravtsov A. V., Klypin A. A., Nagai D., 2004, ApJ, 616, 16
Gnedin O. Y., Brown W. R., Geller M. J., Kenyon S. J., 2010, ApJ, 720, L108
Gómez F. A., Besla G., Carpintero D. D., Villalobos Á., O'Shea B. W., Bell E. F., 2015, ApJ, 802, 128
González R. E., Kravtsov A. V., Gnedin N. Y., 2013, ApJ, 770, 96
Grand R. J. J. et al., 2017, MNRAS, 467, 179
Grand R. J. J. et al., 2018, MNRAS, 481, 1726
Han J., Wang W., Cole S., Frenk C. S., 2016a, MNRAS, 456, 1003

Han J., Wang W., Cole S., Frenk C. S., 2016b, MNRAS, 456, 1017
Hellwing W. A., Frenk C. S., Cautun M., Bose S., Helly J., Jenkins A., Sawala T., Cytowski M., 2016, MNRAS, 457, 3492
Huang Y. et al., 2016, MNRAS, 463, 2623
Kafle P. R., Sharma S., Lewis G. F., Bland-Hawthorn J., 2012, ApJ, 761, 98
Kafle P. R., Sharma S., Lewis G. F., Bland-Hawthorn J., 2014, ApJ, 794, 59
Kallivayalil N., van der Marel R. P., Besla G., Anderson J., Alcock C., 2013, ApJ, 764, 161
Kennedy R., Frenk C., Cole S., Benson A., 2014, MNRAS, 442, 2487
Klypin A., Kravtsov A. V., Valenzuela O., Prada F., 1999, ApJ, 522, 82
Koposov S. E., Rix H.-W., Hogg D. W., 2010, ApJ, 712, 260
Küpper A. H. W., Balbinot E., Bonaca A., Johnston K. V., Hogg D. W., Kroupa P., Santiago B. X., 2015, ApJ, 803, 80
Li Y.-S., White S. D. M., 2008, MNRAS, 384, 1459
Li Z.-Z., Jing Y. P., Qian Y.-Z., Yuan Z., Zhao D.-H., 2017, ApJ, 850, 116
Lovell M. R., Frenk C. S., Eke V. R., Jenkins A., Gao L., Theuns T., 2014, MNRAS, 439, 300
Lu Y., Mo H. J., Katz N., Weinberg M. D., 2006, MNRAS, 368, 1931
Ludlow A. D., Navarro J. F., Angulo R. E., Boylan-Kolchin M., Springel V., Frenk C., White S. D. M., 2014, MNRAS, 441, 378
Matthee J., Schaye J., Crain R. A., Schaller M., Bower R., Theuns T., 2017, MNRAS, 465, 2381
McConnachie A. W., 2012, AJ, 144, 4
McMillan P. J., 2011, MNRAS, 414, 2446
McMillan P. J., 2017, MNRAS, 465, 76
Monari G. et al., 2018, A&A, 616, L9
Moore B., Ghigna S., Governato F., Lake G., Quinn T., Stadel J., Tozzi P., 1999, ApJ, 524, L19
Navarro J. F., Frenk C. S., White S. D. M., 1996, ApJ, 462, 563
Navarro J. F., Frenk C. S., White S. D. M., 1997, ApJ, 490, 493
Neto A. F. et al., 2007, MNRAS, 381, 1450
Newberg H. J., Willett B. A., Yanny B., Xu Y., 2010, ApJ, 711, 32
Newton O., Cautun M., Jenkins A., Frenk C. S., Helly J. C., 2018, MNRAS, 479, 2853
Patel E., Besla G., Mandel K., 2017, MNRAS, 468, 3428
Patel E., Besla G., Mandel K., Sohn S. T., 2018, ApJ, 857, 78
Pawlowski M. S. et al., 2014, MNRAS, 442, 2362
Peñarrubia J., Fattahi A., 2017, MNRAS, 468, 1300
Peñarrubia J., Gómez F. A., Besla G., Erkal D., Ma Y.-Z., 2016, MNRAS, 456, L54
Pfeffer J., Kruijssen J. M. D., Crain R. A., Bastian N., 2018, MNRAS, 475, 4309
Piatek S., Pryor C., Olszewski E. W., 2016, AJ, 152, 166
Piffl T. et al., 2014, A&A, 562, A91
Planck Collaboration et al., 2014, A&A, 571, A1
Posti L., Helmi A., 2018, A&A, 621, A56
Purcell C. W., Zentner A. R., 2012, J. Cosmol. Astropart. Phys., 12, 007
Rossi E. M., Marchetti T., Cacciato M., Kuiack M., Sari R., 2017, MNRAS, 467, 1844
Schaller M. et al., 2015, MNRAS, 451, 1247
Schaye J. et al., 2015, MNRAS, 446, 521
Schönrich R., Binney J., Dehnen W., 2010, MNRAS, 403, 1829
Shao S., Cautun M., Frenk C. S., Grand R. J. J., Gómez F. A., Marinacci F., Simpson C. M., 2018b, MNRAS, 476, 1796
Shao S., Cautun M., Deason A. J., Frenk C. S., Theuns T., 2018c, MNRAS, 479, 284
Simon J. D., 2018, ApJ, 863, 89
Smith M. C. et al., 2007, MNRAS, 379, 755
Sohn S. T., Besla G., van der Marel R. P., Boylan-Kolchin M., Majewski S. R., Bullock J. S., 2013, ApJ, 768, 139
Sohn S. T., Watkins L. L., Fardal M. A., van der Marel R. P., Deason A. J., Besla G., Bellini A., 2018, ApJ, 862, 52
Springel V. et al., 2008, MNRAS, 391, 1685
Springel V., Yoshida N., White S. D. M., 2001, New Astron., 6, 79
Vasiliev E., 2019, MNRAS, 482, 1525
Vera-Ciro C. A., Helmi A., Starkenburg E., Breddels M. A., 2013, MNRAS, 428, 1696

Wang J., Frenk C. S., Navarro J. F., Gao L., Sawala T., 2012, MNRAS, 424, 2715
Wang W., Han J., Cooper A. P., Cole S., Frenk C., Lowing B., 2015, MNRAS, 453, 377
Wang W., Han J., Cole S., Frenk C., Sawala T., 2017, MNRAS, 470, 2351
Wang W., Han J., Cole S., More S., Frenk C., Schaller M., 2018, MNRAS, 476, 5669
Watkins L. L., Evans N. W., An J. H., 2010, MNRAS, 406, 264
Watkins L. L., van der Marel R. P., Sohn S. T., Evans N. W., 2018, preprint(arXiv: 1804.11348)
Wechsler R. H., Bullock J. S., Primack J. R., Kravtsov A. V., Dekel A., 2002, ApJ, 568, 52
Wetzel A. R., Deason A. J., Garrison-Kimmel S., 2015, ApJ, 807, 49
Wilkinson M. I., Evans N. W., 1999, MNRAS, 310, 645
Xue X. X. et al., 2008, ApJ, 684, 1143
Yencho B. M., Johnston K. V., Bullock J. S., Rhode K. L., 2006, ApJ, 643, 154
Zhu Q., Marinacci F., Maji M., Li Y., Springel V., Hernquist L., 2016, MNRAS, 458, 1559

APPENDIX A: PROBABILITY DISTRIBUTIONS

Here we give a short summary on how to calculate the PDF of one variable that is a function of one or more variables with known PDFs. In our case, we want to know the PDF of M_{200}, given the distributions of either scaled angular momentum, scaled energy, or both scaled angular momentum and energy.

The PDF, $p(u)$, of a variable u, which is a function of x, is given by

$$p(u) = p(x) \left| \frac{\mathrm{d}x}{\mathrm{d}u} \right| , \qquad (A1)$$

where $p(x)$ is the probability of variable x and where the derivative corresponds to the Jacobian of the transformation. In our case, the variable u corresponds to the host halo mass, M_{200}, while x corresponds to either the scaled angular momentum, $\widetilde{L}$, or the scaled energy, $\widetilde{E}$. Replacing these variables into equation (A1), we obtain equations (8) and (9), that is

$$p(M_{200}|\mathbf{x}^s) = F_E(\widetilde{E}) \left. \frac{\partial \widetilde{E}}{\partial M_{200}} \right|_{\widetilde{E}=\widetilde{E}^s} , \qquad (A2)$$

$$p(M_{200}|\mathbf{x}^s) = F_L(\widetilde{L}) \left. \frac{\partial \widetilde{L}}{\partial M_{200}} \right|_{\widetilde{L}=\widetilde{L}^s} . \qquad (A3)$$

To constrain M_{200} using both $\widetilde{E}$ and $\widetilde{L}$, we can extend equation (A1) to the two-dimensional case. However, doing so entails some very involved calculations. We bypassed this step by combining the two one-dimensional cases to infer the two-dimensional expression. If the $\widetilde{E}$ and $\widetilde{L}$ variables would be independent, then we could just multiply the right-hand side terms of equations (A2) and (A3). However, that is not the case, so we need to take the joint probability, $F(\widetilde{E}, \widetilde{L})$. Furthermore, we also need to obtain the correct units, which we achieve by adding an extra M_{200} factor. Putting everything together, we obtain equation (10), that is

$$p(M_{200}|\mathbf{x}^s) = F(\widetilde{E}, \widetilde{L}) \, M_{200} \left. \frac{\partial \widetilde{E}}{\partial M_{200}} \frac{\partial \widetilde{L}}{\partial M_{200}} \right|_{\widetilde{E}=\widetilde{E}^s, \, \widetilde{L}=\widetilde{L}^s} . \qquad (A4)$$

We performed extensive tests of the three likelihoods, equations (A2)–(A4), to find that they give very robust estimates of the total mass of haloes.

APPENDIX B: MASS DEPENDENCE OF SCALED ENERGY AND ANGULAR MOMENTUM

Here we test the host halo mass independence of the scaled energy and angular momentum of satellites. We take all the luminous satellites in the EAGLE simulation and scale their orbital energy and orbital angular momentum according to equation (5), that is $\propto M_{200}^{2/3}$, where M_{200} is the host mass. The resulting distributions are shown in Fig. B1.

We find that, to a very good approximation, the distributions of $\widetilde{E}$ and $\widetilde{L}$ are indeed the same over at least two orders of magnitude in host mass. There are a few small departures from universality,
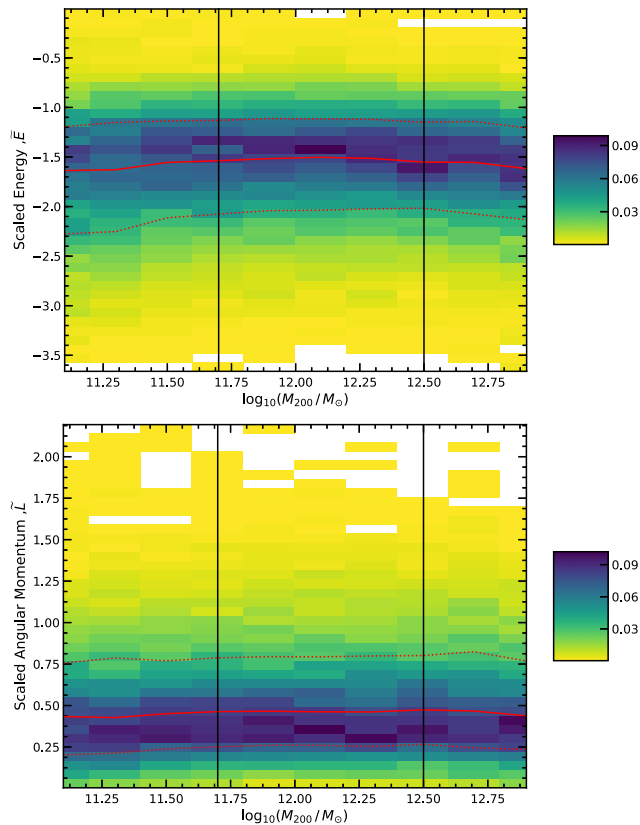
especially for low halo masses. This could be a manifestation of the limited resolution of EAGLE, which resolves only a small fraction of the brightest satellites of $10^{11.2}$ $M_\odot$ haloes. However, this small departure from universality does not affect our results since this work is based on hosts with masses in the range $10^{11.7}$–$10^{12.5}$ $M_\odot$, which corresponds to the region between the two vertical lines in Fig. B1.

APPENDIX C: DEPENDENCE ON CONCENTRATION

In Fig. C1 we show how the MW halo concentration affects our mass estimate. Note that in our method (described in Section 3) we marginalize over the concentration parameter. The coloured lines show the mass estimates from individual satellites and the thick black line the combined mass estimate as a function of the assumed halo concentration. In general, the concentration makes little difference to our estimated masses – this is especially true for the combined mass estimate, which remains flat over a wide range in halo concentration. While not shown, we also find that the maximum likelihood values are largely independent of the assumed concentration. Thus, the 10 classical satellites studied here cannot, on their own, constrain the MW halo concentration. However, as we show in Section 4.2, we can estimate the concentration of the MW halo by combining our total halo mass estimate with determinations of the halo mass in the inner regions of the Galaxy.
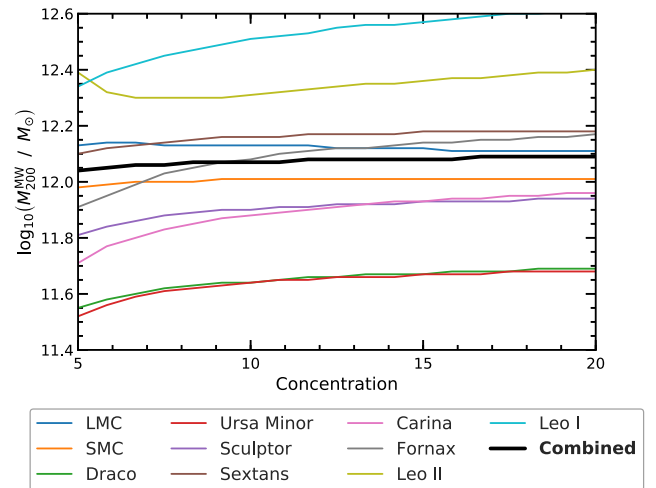

Figure B1. The dependence on host halo mass, M_{200}, of the scaled energy, $\widetilde{E}$ (top panel), and scaled angular momentum, $\widetilde{L}$ (bottom panel), of EAGLE satellites. The colour scale shows the density of points, with darker colours corresponding to higher density regions. The distribution is column normalized to each mass bin to allow easy comparison. The solid lines show the median values as a function of M_{200}, while the dotted lines show the 16 and 84 percentiles of the distribution. The two vertical lines delineate the mass range used in our analysis. The plots show that scaling the energy and angular momentum by $M_{200}^{-2/3}$ leads to quantities that are independent of M_{200} to a very good approximation.

Figure C1. The MW total mass estimate, M_{200}^{MW}, as a function of the assumed concentration of the MW halo. The coloured lines show the mass estimates from individual satellites and the black solid line shows the combined mass estimate. There is a very weak dependence on concentration – this is especially true for the combined mass estimate, which remains flat over a wide range of halo concentration.

APPENDIX D: DISTRIBUTION OF MAXIMUM LIKELIHOODS

The MW classical satellites have at least two atypical properties: (i) they are distributed on a thin plane with many of the satellites rotating within this plane and (ii) the satellites have a very low velocity anisotropy indicative of circularly biased orbits. These two characteristics place the MW satellite system in the 5 per cent and 2 per cent tails of the ΛCDM predictions (Cautun et al. 2015; Cautun & Frenk 2017). This raises the concern that the satellites may also be atypical in terms of their energy or angular momentum distributions. If so, this could lead to biases or untrustworthy MW mass estimates using our method.

A straightforward way to test for this is to compare the maximum likelihood value for the MW with the corresponding values for a large sample of ΛCDM haloes. This is shown in Fig. D1, where we plot the distribution of maximum likelihood values for the EAGLE and AURIGA mock satellite systems. We find very good agreement between the EAGLE and AURIGA mocks and, more importantly, the value for the MW lies in the central region of the ΛCDM expectation. This indicates that we can find a range of M_{200} values for the Galactic halo for which the classical satellites have energy and angular momentum values that are fully consistent with the ΛCDM predictions.
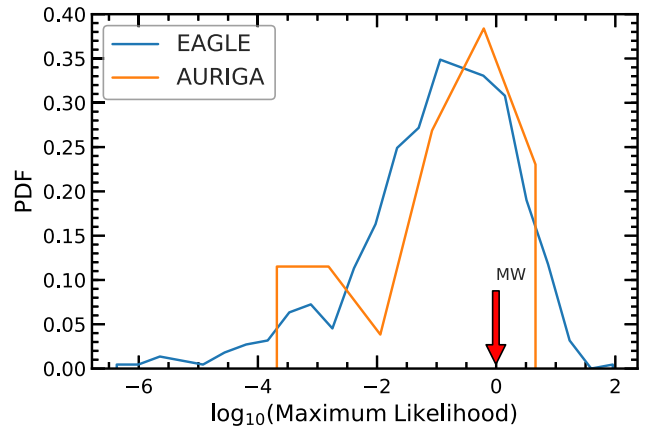

Figure D1. The distribution of maximum likelihood values for the mass determination method based on the energy and angular momentum of satellites. We show results for a sample of $\sim$2500 EAGLE systems and for the 30 AURIGA haloes that have a higher resolution and different galaxy formation models than EAGLE. The downward pointing arrow shows the maximum likelihood corresponding to the MW mass determination, which is fully consistent with the EAGLE and AURIGA distributions. This indicates that the MW is not an atypical system in terms of its satellites' energy and angular momentum, and thus we can trust our MW mass determination.

This paper has been typeset from a TeX/LaTeX file prepared by the author.